

# Self-Similar Evolution of Cosmic-Ray-Modified Quasi-Parallel Plane Shocks

Hyesung Kang<sup>a</sup> T. W. Jones<sup>b</sup>

<sup>a</sup>*Pusan National University, Pusan 609-735, Korea*

<sup>b</sup>*University of Minnesota, Minneapolis, MN 55455, USA*

---

## Abstract

Using an improved version of the previously introduced CRASH (Cosmic Ray Acceleration SHock) code, we have calculated the time evolution of cosmic-ray (CR) modified quasi-parallel plane shocks for Bohm-like diffusion, including self-consistent models of Alfvén wave drift and dissipation, along with “thermal leakage injection” of CRs. The new simulations follow evolution of the CR distribution to much higher energies than our previous study, providing a better examination of evolutionary and asymptotic behaviors. The postshock CR pressure becomes constant after quick initial adjustment, since the evolution of the CR partial pressure expressed in terms of a momentum similarity variable is self-similar. The shock precursor, which scales as the diffusion length of the highest energy CRs, subsequently broadens approximately linearly with time, independent of diffusion model, so long as CRs continue to be accelerated to ever-higher energies. This means the nonlinear shock structure can be described approximately in terms of the similarity variable,  $x/(u_s t)$ , where  $u_s$  is the shock speed once the postshock pressure reaches an approximate time asymptotic state. As before, the shock Mach number is the key parameter determining the evolution and the CR acceleration efficiency, although finite Alfvén wave drift and wave energy dissipation in the shock precursor reduce the effective velocity change experienced by CRs, so reduce acceleration efficiency noticeably, thus, providing a second important parameter at low and moderate Mach numbers. For low Mach numbers ( $M_0 \lesssim 5$ ) the CR acceleration efficiency depends on the thermal leakage injection rate, the Alfvénic Mach number, and any preexisting CR population. However, these dependences become weak for high shock Mach numbers of  $M_0 > 30$ . To evaluate CR acceleration efficiencies in the simulated shocks we present for a wide range of shock parameters a “CR energy ratio”,  $\Phi(M_0)$ , comparing the time asymptotic volume-integrated energy in CRs to the time-integrated kinetic energy flux through the shock. This ratio asymptotes to roughly 0.5 for sufficiently strong shocks. The postshock CR pressure is also approximately 1/2 the momentum flux through the shock for very high Mach numbers.

*Key words:* Cosmic-rays, Diffusive shock acceleration, Numerical hydrodynamics

## 1 Introduction

Astrophysical plasmas, from the interplanetary gas inside the heliosphere to the galaxy intracluster medium (ICM), are magnetized and turbulent and contain nonthermal particles in addition to gas thermal particles. So, understanding complex interactions among these different components is critical to the study of many astrophysical problems. In collisionless shocks entropy is generated via collective electromagnetic viscosities, i.e., interactions of charged particles with turbulent fields [36]. Some suprathermal particles of the shock heated gas can leak upstream, their streaming motions against the background fluid exciting MHD Alfvén waves upstream of the shock [6,32]. Then those particles can be further accelerated to very high energies through multiple shock crossings resulting from resonant scatterings with the self-excited Alfvén waves in the flows converging across the shock [13,10,36].

Detailed nonlinear treatments of diffusive shock acceleration (DSA) account for incoming thermal particles injected into the CR population (e.g., [19,37,21]) as a consequence of incomplete thermalization by collisionless dissipation processes. Those particles, while relatively few in number, can subsequently accumulate a major fraction of the shock kinetic energy as their individual energies increase [16,26]. Such predictions are supported by a variety of observations including direct measurements of particle spectra at interplanetary shocks, nonthermal  $\gamma$ -ray, X-ray and radio emissions of supernova remnant shocks and also possibly the ICM of some X-ray clusters (e.g., [10,3,41]). CR acceleration may be universal to astrophysical shocks in diffuse, ionized media on all scales.

Unlike an ideal gasdynamic shock, downstream states of a CR modified shock cannot be determined in a straightforward way by simple jump conditions across the shock front. This is because the shock transition depends on the CR pressure distribution upstream of the dissipative subshock. The particle acceleration takes place on diffusion time and length scales ( $t_d(p) = \kappa(p)/u_s^2$  and  $l_d(p) = \kappa(p)/u_s$ , where  $\kappa(p)$  is diffusion coefficient and  $u_s$  is the shock speed), which are much larger than the shock dissipation scales. Unless or until some boundary condition limits the maximum CR momentum, this structure will continue to evolve along with the CR distribution. Thus the evolution of a CR

---

*Email addresses:* kang@uju.es.pusan.ac.kr (Hyesung Kang),  
twj@astro.umn.edu (T. W. Jones).

*URL:* www.astro.umn.edu/~twj (T. W. Jones).

shock with a finite age and size should properly be followed by time-dependent numerical simulations. In addition, complex interplay among CRs, resonant waves, and the underlying gas flow (i.e., thermal leakage injection, self-excited waves, resonant scatterings of particles by waves, and non-linear feedback to the gas flow) is model dependent and not yet understood completely.

In the time dependent kinetic equation approach to numerical study of CR acceleration at shocks, the diffusion-convection equation for the particle momentum distribution,  $f(p, x, t)$ , is solved, along with suitably modified gasdynamic equations (e.g., [25]). Since accurate solutions to this equation require a computational grid spacing smaller than the particle diffusion length,  $l_d(p)$ , and since realistic diffusion coefficients have steep momentum dependence, a wide range of length scales must be resolved in order to follow the CR acceleration from the injection momentum (typically  $p_{\text{inj}}/m_p c \sim 10^{-2}$ ) to highly relativistic momenta ( $p/m_p c \gg 1$ ). This constitutes an extremely challenging numerical task, which can require rather extensive computational resources, especially if one allows temporal and spatial evolution of diffusion behavior. To overcome this numerical problem in a generally applicable way we have built the CRASH (Cosmic-Ray Acceleration SHock) code by implementing Adaptive Mesh Refinement (AMR) techniques and subgrid shock tracking methods [25,30] in order to enhance computational efficiency. The CRASH code also treats thermal leakage injection self-consistently by adopting a shock transparency function for suprathermal particles in the shock [26].

We previously applied our CRASH code in a plane-parallel geometry to calculate the nonlinear evolution of CR modified shocks in the absence of significant local Alfvén wave heating and advection [26,27,29]. For those models the shock sonic Mach number,  $M_0$ , largely controlled the thermal leakage injection rate and the CR acceleration efficiency in evolving modified planar shocks, since  $M_0$  determines the relative velocity jump across the shock and consequently the degree of shock modification by CRs. In all but some of the highest Mach number shocks the CR injection rate and the postshock CR pressure approached time-asymptotic values when a balance was achieved between acceleration/injection and diffusion/advection processes. This resulted in an approximate “self-similar” flow structure, in the sense that the shock structure broadened approximately linearly in time, so that the shock structure could be expressed in terms of the similarity coordinate  $u_s t$ . It is likely that all of the models would have reached such asymptotic dynamical structures eventually, but performance limits in the version of the code in use at that time prevented us from extending some of the simulations long enough to confirm that. The CR distribution evolved only to  $p_{\text{max}}/m_p c \sim 10 - 10^3$ . Based on the self-similar evolution reported in our previous work, we calculated the ratio of CR energy to inflowing kinetic energy,  $\Phi$ , (see Eq. [12] below) as a measure of the CR acceleration efficiency in a time-asymptotic limit. The CR energy ratio,  $\Phi$ , increased with the shock Mach number, but approached  $\approx 0.5$

for large shock Mach numbers,  $M_0 > 30$ , and it was relatively independent of other upstream properties or variation in the injection parameter. In those shocks where we observed time asymptotic dynamical behaviors the postshock CR pressures were  $\sim 30 - 60\%$  of the ram pressure in the initial shock frame, this ratio increasing with Mach number. For some of the highest Mach number shocks in that study CR pressure continued to increase to the end of the simulation, so the final values could not be measured. Finally, the presence of a preexisting, upstream CR population was seen in those earlier simulations to be equivalent to having slightly more efficient thermal leakage injection for such strong shocks, while it could substantially increase the overall CR energy in moderate strength shocks with  $M_0 < 3$ .

In the present paper, we revisit the problem of self-similar evolution of CR modified shocks with a substantially improved numerical scheme that enables us to follow the particle acceleration to energies much higher than we considered before. This allows us to measure asymptotic dynamical properties for all the newly simulated shocks and to demonstrate that the self-similar evolution of the CR partial pressure in terms of a momentum similarity variable leads to the constancy of the postshock CR pressure. We also include in the new work the effects of Alfvén wave drift and dissipation in the shocks. The time asymptotic CR acceleration efficiency is once again controlled by the shock Mach number but diminished as the ratio of Alfvénic Mach number to sonic Mach number decreases. The asymptotic shock properties are largely independent of the magnitude of the spatial diffusion coefficient and also its subrelativistic momentum dependence.

The basic equations and details of the numerical method are described in §2. We present simulation results for a wide range of shock parameters in §3, followed by a summary in §4.

## 2 Numerical Method

### 2.1 Basic Equations

The evolution of CR modified shocks depends on a coupling between the gasdynamics and the diffusive CRs. That coupling takes place by way of resonant MHD waves, although it is customary to express the pondermotive wave force and dissipation in the plasma through the associated CR pressure distribution properties along with a characteristic wave propagation speed (usually the Alfvén speed) (e.g., [42,1]). Consequently, in our simulations we solve the standard gasdynamic equations with CR pressure terms added in the conservative, Eulerian formulation for one dimensional plane-parallel geometry. The

evolution of a modified entropy,  $S = P_g/\rho^{\gamma_g-1}$ , is followed everywhere except across the subshock, since for strongly shocked flows, numerical errors in computing the gas pressure from the total energy can lead to spurious entropy generation with standard methods, especially in the shock precursor [26].

$$\frac{\partial \rho}{\partial t} + \frac{\partial(u\rho)}{\partial x} = 0, \quad (1)$$

$$\frac{\partial(\rho u)}{\partial t} + \frac{\partial(\rho u^2 + P_g + P_c)}{\partial x} = 0, \quad (2)$$

$$\frac{\partial(\rho e_g)}{\partial t} + \frac{\partial}{\partial x}(\rho e_g u + P_g u) = -u \frac{\partial P_c}{\partial x} \quad (3)$$

$$\frac{\partial S}{\partial t} + \frac{\partial}{\partial x}(Su) = + \frac{(\gamma_g - 1)}{\rho^{\gamma_g-1}} [W(x, t) - L(x, t)], \quad (4)$$

where  $P_g$  and  $P_c$  are the gas and the CR pressure, respectively,  $e_g = P_g/[\rho(\gamma_g - 1)] + u^2/2$  is the total energy of the gas per unit mass. The remaining variables, except for  $L$  and  $W$  have standard meanings. The injection energy loss term,  $L(x, t)$ , accounts for the energy carried by the suprathermal particles injected into the CR component at the subshock and is subtracted from the postshock gas immediately behind the subshock. Gas heating due to Alfvén wave dissipation in the upstream region is represented by the term  $W(x, t) = -v_A \partial P_c / \partial x$ , where  $v_A = B/\sqrt{4\pi\rho}$  is the Alfvén speed. This commonly used dissipation expression derives from a quasi-linear model in which Alfvén waves are amplified by streaming CRs and dissipated locally as heat in the precursor region (e.g., [22]).

The CR population is evolved by solving the diffusion-convection equation in the form,

$$\frac{\partial g}{\partial t} + (u + u_w) \frac{\partial g}{\partial x} = \frac{1}{3} \frac{\partial}{\partial x} (u + u_w) \left( \frac{\partial g}{\partial y} - 4g \right) + \frac{\partial}{\partial x} [\kappa(x, y) \frac{\partial g}{\partial x}], \quad (5)$$

where  $g = p^4 f$ , with  $f(p, x, t)$  the pitch angle averaged CR distribution, and where  $y = \ln(p)$ , while  $\kappa(x, p)$  is the spatial diffusion coefficient [42]. For simplicity we always express the particle momentum,  $p$  in units  $m_p c$  and consider only the proton CR component. The wave speed is set to be  $u_w = v_A$  in the upstream region, while we use  $u_w = 0$  in the downstream region. This term reflects the fact that the scattering by Alfvén waves tends to isotropize the CR distribution in the wave frame rather than the bulk-flow, gas frame [42]. Upstream, the waves are expected to be dominated by the streaming instability, so face upwind. Behind the shock, various processes, including wave reflection, are expected to lead to a more nearly isotropic wave field (e.g., [2]).

Eqs. (1)-(5) are simultaneously integrated by the CRASH code in plane-parallel geometry. The detailed numerical description can be found in Kang et al. 2002 [26]. A key performance feature of the CRASH code is multiple levels of refined grids (typically  $l_g = 8 - 10$ ) strategically laid around the subshock to resolve the diffusion length scale of the lowest energy particles near injection momenta. Grid refinement spans a region around the subshock just large enough to include comfortably the diffusion scales of dynamically important high energy CRs with enough levels to follow freshly injected low energy CRs with sufficient resolution to produce converged evolutionary behaviors. To accomplish grid refinement effectively it is necessary to locate the subshock position exactly. Thus, we track the subshock as a moving, discontinuous jump inside the initial, uniform and fixed grid [25].

## 2.2 Diffusion Model

We considered in this study two common choices for diffusion models. First is the Bohm diffusion model, which represents scattering expected for a saturated wave spectrum and gives what is generally assumed to be the minimum diffusion coefficient as  $\kappa_B = 1/3r_g v$ , when the particles scatter within a path of one gyration radius (i.e.,  $\lambda_{\text{mfp}} \sim r_g$ ). This gives

$$\kappa_B(p) = \kappa_n \frac{p^2}{(p^2 + 1)^{1/2}}. \quad (6)$$

The coefficient  $\kappa_n = mc^3/(3eB) = (3.13 \times 10^{22} \text{cm}^2 \text{s}^{-1}) B_\mu^{-1}$ , where  $B_\mu$  is the magnetic field strength in units of microgauss. There has been much discussion recently about amplification of the large scale magnetic field within the shock precursor (e.g., [32,35,44]). Since physical models of that evolution are still not well developed, we will assume for simplicity in the simulations presented here that the large scale field is constant through the shock structure.

Because of its steep momentum dependence in the nonrelativistic regime, the Bohm diffusion model requires an extremely fine spatial grid resolution whenever nonrelativistic CRs are present. On the other hand the form of  $\kappa(p)$  for nonrelativistic momenta mostly impacts only early evolution of CR-modified shocks, when CR feedback is dominated by nonrelativistic particles and thermal leakage injection rates are adjusting rapidly to changes from initial conditions. So, to concentrate computational effort more efficiently, we adopted in some previous works [25,30] a ‘‘Bohm-like’’ diffusion coefficient that includes a weaker momentum dependence for the non-relativistic regime,

$$\kappa_{BL}(p) = \kappa_n p. \quad (7)$$

According to those previous studies, the differences in results between the two models are minor except during early nonlinear shock evolution, as expected. Thanks to the weaker momentum dependence of  $\kappa_{BL}$  we can, for given computational resources, calculate numerically converged models with smaller  $\kappa_n$  resulting in the acceleration of CRs to higher momenta.

In order to quench the well-known CR acoustic instability in the precursor of highly modified CR shocks (e.g., [24]), we assume a density dependence for the diffusion coefficient,  $(\rho/\rho_0)^{-1}$ , so that  $\kappa(x, p) = \kappa_B(\rho/\rho_0)^{-1}$  or  $\kappa(x, p) = \kappa_{BL}(\rho/\rho_0)^{-1}$ , where  $\rho_0$  is the upstream gas density. This density dependence also models enhancement of the Alfvén wave magnetic field amplitude due to flow compression. We note, also, for clarity that hereafter we use the subscripts '0', '1', and '2' to denote conditions far upstream of the shock, immediately upstream of the gas subshock and immediately downstream of the subshock, respectively.

### 2.3 Thermal Leakage Model

In the CRASH code suprathermal particles are injected as CRs self-consistently via “thermal leakage” through the lowest CR momentum boundary. The thermal leakage injection model emulates the filtering process by which suprathermal particles well into the tail of the postshock Maxwellian distribution leak upstream across the subshock [37,36]. This filtering is managed numerically by adopting a “transparency function”,  $\tau_{\text{esc}}(\epsilon_B, v)$ , that expresses the probability of supra-thermal particles at a given velocity,  $v$ , successfully swimming upstream across the subshock through the postshock MHD waves [21,26]. The one model parameter,  $\epsilon_B = B_0/B_\perp$ , is the ratio of the amplitude of the postshock wave field interacting with the low energy particles,  $B_\perp$ , to the general magnetic field,  $B_0$ , which is aligned with the shock normal in these simulations. The transparency function fixes the lowest momentum of the CR component in our simulations from the condition that  $\tau_{\text{esc}} > 0$  (i.e., non-zero probability to cross the subshock for CRs) for  $p > p_1$ , where  $p_1 = (u_2/c)(1 + \epsilon_B)/\epsilon_B$  and  $u_2$  is the downstream flow speed in the subshock rest frame. Initially  $p_1$  is determined by the downstream speed of the initial shock, but it decreases as the subshock weakens and then it becomes constant after the CR modified shock structures reach asymptotic states.

Since suprathermal particles have to swim against the scattering waves advecting downstream, the subshock Mach number,  $M_s$ , is one of the key shock characteristics that control the injection fraction. Previous simulations showed that injection is less efficient for weaker shocks, but becomes independent of  $M_0$  for strong shocks, when the subshock compression asymptotes [26]. For a given total shock Mach number,  $M_0$ , on the other hand, the injection rate

is controlled mainly by the parameter  $\epsilon_B$ . In practice we have found that  $\epsilon_B \sim 0.2 - 0.25$  leads to an injection fraction in the range  $\sim 10^{-4} - 10^{-3}$ . This is similar to commonly adopted values in other models that employ a fixed injection rate (e.g., [8,33,4]). Although somewhat higher field turbulence values ( $0.25 < \epsilon_B < 0.3$ ) are suggested theoretically for strong shocks [34], these evoke a start-up problem in the numerical simulations, since they lead to very rapid initial injection that cools the postshock flow too strongly for it to remain numerically stable. Once the shock structure becomes nonlinear, however, those influences moderate greatly, so that, as we have shown previously, the ultimate CR acceleration behavior depends only weakly on  $\epsilon_B$ . In fact, we have found previously for strong shocks that the time-asymptotic behaviors are very weakly dependent on  $\epsilon_B$  [25], so its chosen value will have no influence on our final conclusions.

We directly track the fraction of particles injected into the CR population as follows:

$$\xi(t) = \frac{\int dx \int_{p_1}^{p_2} 4\pi f_{\text{CR}}(p, x, t) p^2 dp}{n_0 u_{s,0} t}, \quad (8)$$

where  $f_{\text{CR}}$  is the CR distribution function above  $p_1$ , while  $n_0 u_{s,0} t$  is the number of particles passed through the shock until the time  $t$ . The highest momentum of the CR component,  $p_2$ , is chosen so that it is well above  $p_{\text{max}}$  at the simulation termination time, where  $p_{\text{max}}$  is defined in §2.4.

#### 2.4 CR Acceleration Efficiency

The postshock thermal energy in a gasdynamic shock can, of course, be calculated analytically by the Rankine-Hugoniot jump condition. On the other hand, the CR population and the associated acceleration efficiency at CR modified shocks should properly be obtained through time-dependent integration of the shock structure from given initial states, since the CR distribution depends on the shock structure, which is not discontinuous and continues to evolve so long as the CR population evolves. In particular CR modified shocks contain a smooth precursor in the upstream region whose scale height grows in time in proportion to the diffusion length of energetically dominant particles. The total shock compression may, similarly, evolve over a significant time period. The standard expression for the mean acceleration timescale for a particle to reach momentum  $p$  in the test-particle limit of DSA theory is given by [31]

$$\tau_{\text{acc}}(p) = \frac{3}{u_1 - u_2} \left( \frac{\kappa_1}{u_1} + \frac{\kappa_2}{u_2} \right). \quad (9)$$



In the test particle limit the shock compression is given by the Rankin-Hugoniot condition. Then assuming a  $\gamma_g = 5/3$  gasdynamic shock and a diffusion coefficient taking the density dependence indicated at the end of §2.2, this leads to

$$\tau_{acc}(p) \approx 8 \frac{M_0^2}{M_0^2 - 1} \frac{\kappa(p)}{u_s^2}, \quad (10)$$

where  $u_s$  and  $M_0$  are the shock speed and sonic Mach number, respectively. While this expression should strictly speaking be modified in highly modified CR shocks, since the shock structure and the associated CR transport are more complex than assumed in Eq. (10) [11], we find it empirically to be reasonably consistent with our results described below. Accordingly, we may expect and confirm below that the time-dependent evolution of our CR modified shocks will be determined primarily by the shock Mach number and can be expressed simply in terms of diffusion length and time scales.

Within this model the highest momentum expected to be accelerated in strong shocks by the time  $t$  is set according to Eq. (10) by the relation  $t \approx 8\kappa(p_{\max})/u_s^2$ . In that case the scale height of the precursor or shock transition structure grows linearly with time as

$$l_{\text{shock}} \sim \frac{\kappa(p_{\max})}{u_s} \sim \frac{1}{8} u_s t, \quad (11)$$

independent of the magnitude or the momentum dependence of  $\kappa(p)$ . This evolution should continue until some other physics limits the increase in CR momentum, such as the finite size of the shock system. Since the CR pressure approaches a time-asymptotic value (see Figs. 3-5 below), the evolution of the CR-modified shock becomes, under these circumstances, approximately self-similar, independent of the form of the diffusion coefficient, while  $l_{\text{shock}}$  grows linearly with time [27,28,29]. On the other hand,  $\kappa(p_{\max}) \approx l_{\text{shock}} u_s$ , so for Bohm-like diffusion,  $p_{\max} \approx l_{\text{shock}}(t) u_s / \kappa_n$ . Thus, at a given time the CR distribution,  $g(p)$ , extends for Bohm-like diffusion according to  $p_{\max} \approx u_s^2 t / (8\kappa_n) \propto 1/\kappa_n$ .

Fig. 1 shows a comparison of three models of a  $M_0 = 20$  shock with  $\tilde{\kappa}_B = \tilde{\kappa}_n p^2 / \sqrt{p^2 + 1}$  using  $\tilde{\kappa}_n = 0.1$ , and with  $\tilde{\kappa}_{BL} = \tilde{\kappa}_n p$  using  $\tilde{\kappa}_n = 10^{-4}$  and  $10^{-6}$  in units defined in the following section. The upper left panel, displaying the evolution of postshock CR pressure, demonstrates similar time-asymptotic values for all three models. At early times the CR pressure evolution depends on details of the model, including numerical properties such as spatial and momentum grid resolutions, and the previously described injection suppression scheme used to prevent start up problems.

The other panels in Fig. 1 illustrate shock structure comparisons for the three models at the end of the simulations. The shock structures,  $\rho(x)$  and  $P_c(x)$ , are very similar, while the CR spectrum extends to different values of  $p_{\max}$ , inversely proportional to  $\tilde{\kappa}_n$ .

The self-similar evolution of CR modified shocks makes it useful to apply the ratio of CR energy to a fiducial kinetic energy flux through the shock as a simple measure of acceleration efficiency; namely,

$$\Phi(t) = \frac{\int E_c(x, t) dx}{0.5 \rho_0 u_{s,0}^3 t}. \quad (12)$$

More specifically, this compares the total CR energy within the simulation box to the kinetic energy in the *initial shock frame* that has crossed the shock at a given time. As the shock structures approach time-asymptotic forms the above discussion suggests that  $\Phi(t)$  also may approach time-asymptotic values. This is confirmed in our simulations. We see also that the asymptotic  $\Phi$  values depend in our simulations primarily on shock sonic Mach number and are independent of  $\kappa$ .

The highest momenta achieved in our simulations are set by practical limits on computation time controlled by the vast range of diffusion times and lengths to be modeled. Still, the asymptotic acceleration efficiency ratio is almost independent of the maximum momentum reached. For the three models shown in Fig. 1, for example,  $p_{\max} \sim 10, 10^4, \text{ and } 10^6$  at  $\tilde{t} = 10$ , depending on the value of  $\kappa_n$ , but the CR energy ratio approaches similar values of  $\Phi \sim 0.4$  for all three models.

### 3 Simulation Set Up and Model Parameters

#### 3.1 Units and Initial Conditions

The expected evolutionary behaviors described above naturally suggest convenient units. For example, given a suitable velocity scale,  $\hat{u}$ , and length scale,  $\hat{x}$ , a time scale  $\hat{t} = \hat{x}/\hat{u}$  and diffusion coefficient scale,  $\hat{\kappa} = \hat{x}\hat{u} = \hat{u}^2\hat{t}$  are implied. Alternatively, one can select the velocity scale along with a convenient scale for the diffusion coefficient,  $\hat{\kappa}$ , leading to a natural length scale,  $\hat{x} = \hat{\kappa}/\hat{u}$  and a related time scale,  $\hat{t} = \hat{\kappa}/\hat{u}^2 = \hat{x}/\hat{u}$ . We will follow the latter convention in our discussion. In addition, given an arbitrary mass unit,  $\hat{m}$ , which we take to be the proton mass, we can similarly normalize mass density in terms of  $\hat{\rho} = \hat{m}/\hat{x}^3$ . Pressure is then expressed relative to  $\hat{\rho}\hat{u}^2$ . For clarity we henceforth

indicate quantities normalized by the above scales using a tilde; for example,  $\tilde{u}$ ,  $\tilde{t}$ , and  $\tilde{\kappa}_n$ .

We start each simulation with a pure gasdynamic, right-facing shock at rest in the computational grid. We use the upstream gas speed in this frame,  $u_0$  as our velocity scale, so that the initial, normalized shock speed is  $\tilde{u}_{s,0} = 1$  with respect to the upstream gas. The upstream gas is specified with one of two temperature values, either  $T_0 = 10^4\text{K}$  or  $T_0 = 10^6$ , which represent warm or hot phase of astrophysical diffuse media, respectively. In astrophysical environments, for example, photoionized gas of  $10^4$  K is quite common. Hot and ionized gas of  $> 10^6$  K is also found in the hot phase of the ISM [38,43]. The shock speed and the upstream temperature are related through the sonic Mach number,  $M_0$ , by the usual relation  $u_{s,0} = c_{s,0}M_0 = 15 \text{ km s}^{-1}(T_0/10^4)^{1/2}M_0 = u_0$ , where  $c_{s,0}$  is the sound speed of the upstream gas. So, by choosing  $T_0$  and  $M_0$ , we set the physical value of the shock speed, which, in turn, determines the postshock thermal behavior. For CR distribution properties it is also necessary to define the speed of light,  $c$ , in terms of  $\beta_k = u_0/c$ . The normalized upstream gas density is set to unity; i.e.,  $\tilde{\rho}_0 = 1$ .

The preshock pressure is determined by the shock Mach number,  $\tilde{P}_{g,0} = (1/\gamma_g)M_0^{-2}$ , where the gas adiabatic index,  $\gamma_g = 5/3$ . The postshock states for the initial shocks are determined by the Rankine-Hugoniot shock jump condition. For models with  $T_0 = 10^4\text{K}$ ,  $M_0 = 10-80$  is considered, since the gas would not be fully ionized at slower shocks ( $u_s < 150 \text{ km s}^{-1}$ ), the postshock gas would often become radiative and the CR acceleration become inefficient owing to wave dissipation from ion-neutral collisions (e.g., [15]). For models with  $T_0 = 10^6\text{K}$   $M_0 = 2 - 30$  ( $300 \text{ km s}^{-1} \leq u_s \leq 4500 \text{ km s}^{-1}$ ) is considered, since the CR acceleration should be relatively independent of  $T_0$  for shocks with  $M_0 > 30$ .

In order to explore effects of pre-existing CRs, we also consider, as we did in our earlier work, models with  $T_0 = 10^6$  K that include an ambient (upstream) CR population,  $f(p) \propto p^{-5}$  for  $p_1 \leq p \leq p_2$  and set its pressure  $P_{c,0} = (0.25 - 0.3)P_{g,0}$ . For these models, we adopt  $\kappa_B = 0.1p^2/\sqrt{p^2 + 1}$ ,  $p_1 = (u_{s,0}/c)(1 + \epsilon_B)/\epsilon_B$  and  $p_2 = 10^3$ . For strong shocks the presence of pre-existing CRs is similar in effect to having a slightly higher injection rate, so the time asymptotic shock structure and CR acceleration efficiency depend only weakly on such a pre-existing CR population [26,28]. On the other hand, for weak shocks, a pre-existing CR pressure comparable to the upstream gas pressure represents a significant fraction of the total energy entering the shock, so pre-existing CRs obviously have far more impact. In addition, the time asymptotic CR acceleration efficiency in weak shocks depends sensitively on the injection rate, so increases with increased shock transparency, controlled through  $\epsilon_B$  (see §2.3). Hence, as we found in [29], we expect relatively weak CR shocks ( $M_0 < 5$ ) to be substantially altered by the presence of a finite

upstream  $P_c$ .

### 3.2 Wave Drift and Heating

As shown in earlier works (e.g., [22,30] and references cited therein), the CR acceleration becomes less efficient when Alfvén wave drift and heating terms are included in the simulations. This behavior comes from two effects previously mentioned in §2.1, both of which derive from the resonance interaction between CRs and Alfvén waves in the shock precursor. The Alfvén waves stimulated by CR streaming in the precursor will propagate in the upstream direction, so that the effective advection speed of the CRs into the subshock is reduced. In addition, if the energy extracted from CRs to amplify these waves is locally dissipated, the heating rate in the precursor is increased with respect to the adiabatic rate, so that gas entering the subshock is relatively hotter, and the subshock strength is accordingly reduced. The significance of the effects depends on the sonic Mach number,  $M_0$ , relative to the shock Alfvénic Mach number,  $M_A = u_s/v_A$ ; i.e., on the ratio of the Alfvén speed to the sound speed (see §3.4). In a parallel shock we can write  $M_0/M_A = v_A/c_s = \sqrt{2\theta/[\gamma_g(\gamma_g - 1)]}$ , where we introduce a convenient “Alfvén parameter” as follows,

$$\theta = \frac{E_{B,0}}{E_{th,0}} = (\gamma_g - 1) \frac{P_{g,0}}{P_{B,0}} = \frac{(\gamma_g - 1)}{\beta_p}. \quad (13)$$

This expresses the relative upstream Alfvén and sound speeds in terms of the magnetic to thermal energy density ratio. The parameter  $\beta_p$  is the usual “plasma  $\beta$ ” parameter. For  $\gamma_g = 5/3$ ,  $\beta_p = 2/(3\theta)$ , and  $\theta = (5/9)(M_0/M_A)^2$ . We emphasize for clarity that the present simulations are of parallel shocks, so that the direct dynamical role of the magnetic field has been neglected. Observed or estimated values are typically  $\theta \sim 0.1$  for intracluster media and  $\theta \sim 1$  for the interstellar medium of our Galaxy (e.g., [5,12]). So we consider  $0.1 \leq \theta \leq 1$ , and we will provide comparison to the weak field limit,  $\theta = 0$ . Fig. 2 concisely illustrates the importance of Alfvén wave drift and heating effects on a Mach 10 shock. One can see that the postshock CR pressure, for example, decreases by more than a factor two when the sonic and Alfvén Mach numbers become comparable. Most of the model results we show here used  $\theta = 0.1$ . For the Mach 10 shocks illustrated in Fig. 2 the associated wave terms have reduced the asymptotic CR pressure by about 30% with  $\theta = 0.1$  compared to the shock with no such terms included.

### 3.3 Grid Resolution and Convergence

According to our previous studies [23], the spatial grid resolution should be much finer than the diffusion length of lowest energy particles near the injection momenta, i.e.,  $\Delta x \lesssim 0.1l_d(p_{\text{inj}})$ . Kang & Jones (2006), however, showed that the spherical, comoving CRASH code achieve good numerical convergence, even when  $\Delta x > l_d(p_{\text{inj}})$ . This was due to the fact in the execution of that code the gas subshock remains consistently inside the same comoving grid zone. In order to gain this benefit for our present simulations, we have modified our plane-parallel CRASH code so that the shock is again forced to remain inside the same refined grid zone by regularly redefining the underlying Eulerian grid. The simulations employ eight levels of refinement with the grid spacing reduced by an integer factor of two between refinement levels. The spatial grid resolution on the coarsest, base grid is  $\Delta\tilde{x}_0 = 2 \times 10^{-3}$ , while on the finest, 8<sup>th</sup>, grid  $\Delta\tilde{x}_8 = 7.8 \times 10^{-6}$ . With  $\tilde{\kappa}_n = 10^{-6}$ , the diffusion length for injection momenta  $p_1 \approx 10^{-2}$  becomes  $\tilde{l}_d \approx 10^{-8}$  for models with Bohm-like diffusion,  $\kappa_{BL}$ . Although  $\Delta\tilde{x}_8 > \tilde{l}_d(p_{\text{inj}})$ , we confirmed that the new plane-parallel CRASH code also achieves good numerical convergence in the simulations presented here. This improvement enables us to extend these simulations to CR momenta several orders of magnitude greater than those discussed in [29].

When solving the diffusion-convection equation, we used 230 - 280 uniformly spaced logarithmic momentum bins in the interval  $y = \ln p = [\ln p_1, \ln p_2]$ .

### 3.4 Results

We show in Fig. 3 the time evolution of a  $M_0 = 10$  shock with  $T_0 = 10^6\text{K}$ ,  $\tilde{\kappa}_{BL} = 10^{-6}p$ , and  $\theta = 0.1$ . The wave amplitude parameter in the thermal leakage model was assumed to be  $\epsilon_B = 0.2$ , unless stated otherwise. The lower left panel follows evolution of the volume integrated CR distribution function relative to the total number of particles (mostly in the thermal population) that have passed through the shock, i.e.,  $G(p)/(n_0 u_{s,0} t)$ , where  $G(p) = \int dx g(x, p)$ . As the CR pressure increases in the precursor in response to thermal leakage injection at the subshock and subsequent Fermi acceleration, the subshock weakens. The injection process is self-regulated in such a way that the injection rate reaches and stays at a nearly stable value after quick initial adjustment. Consequently, the postshock CR pressure reaches an approximate time-asymptotic value once a balance is established between fresh injection/acceleration and advection/diffusion of the CR particles away from the shock.

The CR pressure is calculated as

$$P_c = \frac{4\pi}{3} m_p c^2 \int_{p_1}^{p_2} g(p) \frac{p}{\sqrt{p^2 + 1}} d \ln p, \quad (14)$$

so we define  $D(p) \equiv g(p)p/\sqrt{p^2 + 1}$  as a ‘partial pressure function’. The upper left panel of Fig. 4 shows the evolution of  $D(p, x_s)$  at the subshock for the model shown in Fig. 3. Since  $D(p)$  stretches self-similarly in momentum space, we define a new momentum similarity variable as

$$Z \equiv \frac{\ln(p/p_1)}{\ln[p_{\max}(t)/p_1]}. \quad (15)$$

The lowest momentum  $p_1$  becomes constant after the subshock structure becomes steady. The momentum at which numerical values of  $D(p)$  peaks is chosen as  $p_{\max}(t)$  and similar to what is estimated approximately by applying the test-particle theory in §2.4. For the model shown in Fig. 3,  $p_1 \approx 0.01$  and  $p_{\max} \approx 7.27 \times 10^4 \tilde{t}$ .

We then define another ‘partial pressure function’,

$$F(Z) \equiv g(Z) \frac{p}{\sqrt{p^2 + 1}} \ln[p_{\max}(t)/p_1] = D(Z) \ln[p_{\max}(t)/p_1]. \quad (16)$$

Its time evolution is shown as a function of  $Z$  at the upper right panel of Fig. 4. The plot demonstrates that the evolution of  $F(Z)$  becomes self-similar for  $\tilde{t} \geq 2$ . Since  $P_c \propto \int_{p_1} D(p) d \ln p \propto \int_0 F(Z) dZ$ , the areas under the curves of  $D(p)$  or  $F(Z)$  in Fig. 4 represent the CR pressure at the shock. So the self-similar evolution of  $F(Z)$  implies the constancy of  $P_{c,2}$ . In this case  $\tilde{P}_{c,2} \approx 0.31$  for  $\tilde{t} \gtrsim 2$ . From that time forward the spatial distribution of  $P_c$  expands approximately linearly with time, as anticipated in §2.4. This demonstrates that the growth of a precursor and the shock structure proceed approximately in a self-similar way once the postshock CR pressure becomes constant. In the lower panels of Fig. 4 we also show the evolution of  $D(p)$  and  $F(Z)$  for another model with  $M_0 = 50$ ,  $T_0 = 10^4 \text{K}$ ,  $\tilde{\kappa}_B = 0.01p/\sqrt{p^2 + 1}$  and  $\theta = 0.1$ . For the this model  $p_1 \approx 2.0 \times 10^{-3}$  and  $p_{\max} \approx 10\tilde{t}$ . In this case, the CR pressure is mostly dominated by relativistic particles.

Fig. 5 compares the CR distributions at  $\tilde{t} = 10$  for two sets of models spanning a range of sonic Mach numbers for different diffusion model choices. For the simulations represented on the left, the diffusion coefficient is Bohm-like, with  $\tilde{\kappa}_{BL} = 10^{-6}p$  and  $T_0 = 10^6 \text{K}$ . The results on the right come from a Bohm diffusion model with  $\tilde{\kappa}_B = 0.01p^2/\sqrt{p^2 + 1}$  and  $T_0 = 10^4 \text{K}$ . For all models in this figure,  $\theta = 0.1$  and  $\epsilon = 0.2$ . The top panels show the CR distributions

at the shock,  $g(p, x_s) = p^4 f(p, x_s)$ , while the middle panels show the spatially integrated  $G(p)$ . The slopes of the integrated spectra,  $q = -d(\ln G_p)/d \ln p + 4$ , are shown in the bottom panels. For strong shocks with  $M_0 \geq 10$ , both  $p^4 f(p, x_s)$  and  $G(p)$  exhibit concave curvature at high momentum familiar from previous studies e.g., [9,36,4]. The hardened high momentum slopes reflect the fact that higher momentum CRs have longer mean free scattering paths, so encounter an increased compression across the shock precursor and a greater velocity jump.

It is interesting to note in Fig. 5 that the spatially integrated spectra in the stronger shocks show more obvious hardening at high momenta than do the spectra measured at the subshock. This is another consequence of the fact that  $l_d(p)$  increases with momentum, so that the CR spectrum hardens considerably as one measures it further upstream of the subshock. CRs escaping upstream from such a shock would be dominated by the highest momentum particles available.

Fig. 6 compares the evolution of shock properties for the same set of models whose CR spectra are shown in Fig. 5. The evolution of density increase through the precursor,  $\sigma_p = \rho_1/\rho_0$ , and the total compression,  $\sigma_t = \rho_2/\rho_0$ , are shown in each top panel. Compression through the subshock itself can be found through the ratio  $\sigma_s = \rho_2/\rho_1$ . We will discuss shock compression results in more detail below.

The middle panels of Fig. 6 show evolution of the postshock gas and CR pressures normalized to the ram pressure at the initial shock. After fast evolution at the start, these ratios approach constant values for  $\tilde{t} \gtrsim 1$ . The bottom panels monitor the thermal leakage injection fraction,  $\xi(t)$ . With the adopted value of  $\epsilon_B = 0.2$ , the time asymptotic value of this fraction is  $\xi \sim 10^{-4} - 10^{-3}$  with the higher values for stronger shocks. We note that the behavior of  $\xi$  during the early phase ( $\tilde{t} < 1$ ) is controlled mainly by the injection suppression scheme used to prevent start up problems. If the diffusion of particles with lowest momenta near  $p_1$  is better resolved with a finer grid spacing, one may observe some initial reduction of  $\xi(t)$  as the subshock weakens in time (e.g., Fig. 6 of [26]). The various plots show that postshock properties approach time-asymptotic states that depend on the shock Mach number. Generally, as is well known, the shock compression, the normalized postshock CR pressure and the thermal leakage injection fraction increase with shock Mach number. Nonlinear effects, illustrated here by increased shock compression and diminished postshock gas pressure, are relatively unimportant for Mach numbers less than 10 or so. At high Mach number upstream gas temperature is relatively unimportant. In addition, noting that the simulations in the left and right panels employed different models for the low momentum diffusion coefficient, the similarity between the analogous left and right plots illustrate the point made earlier that asymptotic dynamical behaviors are insensitive to

details in the diffusion coefficient.

The Mach number dependences of several important shock dynamical properties are illustrated in Fig. 7. These include the time-asymptotic values of  $\sigma_t$ ,  $\sigma_p$ , and the postshock CR and gas pressures, both normalized by the initial momentum flux,  $\rho_0 u_{s,0}^2$ . Dotted lines provide for comparison the  $\gamma_g = 5/3$  gasdynamic compression ratio and postshock pressure. The strong shock limits of the gasdynamic compression ratio and normalized postshock pressure are 4 and 0.75, respectively. The two sets of models shown in Figs. 5-6 are shown, along with an additional set of models with  $T_0 = 10^6\text{K}$ ,  $\kappa_{BL} = 10^{-6}p$ ,  $\theta = 0.1$ , and  $\epsilon_B = 0.25$ . The normalized postshock CR pressure increases with  $M_0$ , asymptoting towards  $\tilde{P}_{c,2} \sim 0.5$  at high Mach numbers. These values are reduced  $\sim 30\%$  from the analogous results presented in [29], which is consistent with the comparison for the Mach 10 shock shown in Fig. 2. The normalized gas pressure simultaneously drops in response to increases in  $\tilde{P}_c$ , as one would anticipate. It is notable that it actually falls well below 0.25, where one might naively expect it to asymptote in order to maintain a constant total postshock pressure with respect to  $\rho_0 u_{s,0}^2$ . Instead it falls as  $\tilde{P}_{g,2} = P_{g,2}/(\rho_0 u_{s,0}^2) \sim 0.4(M_0/10)^{-0.4}$ , without flattening at high Mach numbers. As we shall see below, this trend is consistent with expected evolution of gas in the precursor. Thus *the total postshock pressure is less than that of a gasdynamic shock of the same initial Mach number,  $M_0$ , despite a softening of the equation of state coming from the CRs.*

For the  $\epsilon_B = 0.2$  cases shown in Fig. 7 the precursor, subshock, and total compression ratios can be approximated by  $\sigma_p \sim 1.5(M_0/10)^{0.29}$ ,  $\sigma_s \sim 3.3(M_0/10)^{0.04}$ , and  $\sigma_t = \sigma_p \sigma_s \sim 4.9(M_0/10)^{0.33}$ , respectively, for  $M_0 \gtrsim 5$ . For these models we also find the subshock Mach number ranges  $3 \lesssim M_1 (= u_1/c_{s,1}) \lesssim 4$  and depends on total Mach number roughly as  $M_1 \propto M_0^{0.1}$ . Since the Rankine-Hugoniot-derived gas shock compression in this Mach number range scales as  $\sigma_s \propto M_1^{0.35}$ , so  $\sigma_s \propto (M_0^{0.1})^{0.35}$  is consistent with the above relation. Although weak, the variation of the subshock strength with full shock sonic Mach number is important to an understanding of the simulated flow behaviors seen in our shock precursors. We note that the subshock behavior seen here in highly modified strong shocks, particularly that it generally evolves towards Mach numbers close to three, is consistent with previous analytic and numerical results, although in some other studies the subshock strength is completely independent of  $M_0$  (e.g., [7,9,36]). The subshock strength in our simulations is determined by complex nonlinear feedback involving the thermal leakage injection process. As noted for the results in Fig. 6 the injection rate,  $\xi$ , generally increases with  $M_0$ . This simultaneously increases  $P_c$ , providing extra Alfvénic heating in the precursor, while cooling gas entering the subshock, as energy is transferred to low energy CRs. It should not be surprising that the balance of these feedback processes is not entirely independent of total Mach number. We comment in passing that the compression values



shown in Fig. 7 depend slightly on  $\epsilon_B$  in the sense that larger values of  $\epsilon_B$  result in a little higher CR injection rate and greater  $P_c$ .

Compression through the shock precursor has been discussed by several previous authors (e.g., [7,8,33,26]). We outline the essential physics to facilitate an understanding of our results. In a steady flow ( $\partial/\partial t = 0$ ) the modified entropy equation (4) can be integrated across the precursor with  $\gamma_g = 5/3$  to give

$$\sigma_p = \frac{\rho_1}{\rho_0} = \left[ \left( \frac{M_1}{M_0} \right)^2 + \frac{2}{3} M_1^2 I \right]^{-3/8}, \quad (17)$$

where  $M_0 = u_{s,0}/c_{s,0}$  and

$$I = \frac{5}{3u_0^3 \rho_0^{1/3}} \int \frac{|W|}{\rho^{2/3}} dx. \quad (18)$$

The same relation can be derived from a Lagrangian perspective applying the second law of thermodynamics to a parcel of gas flowing through the precursor, not necessarily in a steady state. For these simulations  $|W| = |v_A \partial P_c / \partial x|$ . Given the previously mentioned result,  $P_{c,2} = P_{c,1} \sim 0.5 \rho_0 u_s^2$  we can estimate that  $I \approx v_A / u_s \approx 1.34 \sqrt{\theta} / M_0$ . Eq. (17) is then similar to an expression given in [7]. When Alfvén wave dissipation is small, so that  $\theta \ll 5/(4M_0^2)$ , Eq. (17) gives the result  $\sigma_p \sim M_0^{3/4}$ , appropriate for adiabatic compression and consistent with behaviors found in a number of previous analytic and numerical studies (e.g., [7,8,33,26]). For the simulations represented in Figs. 3-7 the opposite limit actually applies, since  $\theta = 0.1 > 5/(4M_0^2)$  whenever  $M_0 > 3.5$ . Then the strong Alfvén dissipation limit of Eq. (17) predicts  $\sigma_p \sim (M_0 \sqrt{\theta})^{3/8} / M_1^{3/4}$ . Substituting our observed relation between subshock Mach number and total Mach number,  $M_1 \propto M_0^{0.1}$ , we establish for fixed  $\theta$  an expected behavior,  $\sigma_p \propto M_0^{0.3}$ , very close to what is observed. If instead of  $\theta$  we had parameterized the Alfvén wave influence in terms of the Alfvénic Mach number, the analogous behavior of Eq. (17) would have been  $\sigma_p \propto 1/(M_A^{3/8} M_1^{3/4})$ . Then for fixed Alfvénic Mach number the precursor compression would vary only with the subshock Mach number, which, has only a weak dependence on the full shock Mach number. That agrees with results presented by [7], for example.

We mention that the precursor/subshock compression properties also explain the observed inverse dependence of postshock gas pressure on initial Mach number. In fact, in a steady flow it is easy to show that

$$\frac{P_{g,2}}{\rho_0 u_0^2} = \frac{2}{(\gamma_g + 1)} \left( 1 - \frac{(\gamma_g - 1)}{2\gamma_g M_1^2} \right) \frac{1}{\sigma_p} \approx \frac{3}{4} \frac{1}{\sigma_p}. \quad (19)$$

Thus we expect an inverse relation between precursor compression and nor-

malized postshock gas pressure, close to what is observed in our simulations.

Finally, Fig. 8 shows time-asymptotic values of the CR energy ratio,  $\Phi(M_0)$ , for models with different  $\theta$  (top panel) and different  $\epsilon_B$  and pre-existing CRs (bottom panel). Models are shown with both  $T_0 = 10^6\text{K}$  and  $T_0 = 10^4\text{K}$ . This figure demonstrates that the CR acceleration depends on the specific model parameters considered here. For models with  $\theta = 0.1$  and  $T = 10^6\text{K}$ , the acceleration efficiency is reduced by up to  $\sim 50\%$  in comparison to models without Alfvén wave drift and dissipation ( $\theta = 0$ ). For larger Alfvén speeds with  $\theta \sim 1$ , the acceleration efficiency is reduced even more significantly as a consequence of strong preshock Alfvénic heating and wave advection. On the other hand, for models with  $T_0 = 10^4\text{K}$  and  $M_0 > 20$  the reduction factor is less than 15% for  $\theta \sim 0.5$ . As shown in previous studies [26,27], larger values of  $\epsilon_B$  lead to higher thermal leakage injection and so more CR energy. Also the presence of preexisting CRs facilitates thermal leakage injection, leading to more injected CR particles and higher acceleration efficiency. Thus, an accurate estimate of the CR energy generated at quasi-parallel shock requires detail knowledge of complex physical processes involved. Fortunately, all these dependences become gradually weaker at higher Mach numbers, and  $\Phi$  tends to approach 0.5 for  $M_0 > 30$ . It seems likely that this asymptotic efficiency would also apply for sufficiently large  $\theta$ . For low Mach number shocks, it is not yet possible to make simple, model-independent efficiency predictions.

#### 4 Conclusion and Summary

While full thermalization takes place instantaneously at a simple, discontinuous jump in an ideal gasdynamic shock, CR acceleration and the corresponding modifications to the underlying flow depend on suprathermal particles passing back and forth diffusively across the shock structure via resonant scatterings with MHD waves. So the time dependent evolution of CR modified shocks depend on complex interactions between the particles, waves in the magnetic field, and underlying plasma flow. These processes develop on the diffusion time scale and diffusion length scale, which are expected to be increasing functions of particle momentum, so CR acceleration and shock evolution rates slow over time. Here we have carried out time-dependent DSA simulations to study the evolution of plane CR modified shocks with quasi-parallel magnetic fields. Simple models for thermal leakage injection and Alfvén wave propagation and dissipation are included. By adopting an underlying base grid that moves with the subshock, our CRASH code with shock tracking and AMR techniques can achieve good numerical convergence at a grid resolution much coarser than that required in a fixed, Eulerian grid. In the comoving grid, the shock remains at the same location, so the compression rate is applied consistently to the CR distribution at the subshock, resulting in much more

accurate low energy CR acceleration.

We showed that the time dependent evolution of CR modified shocks becomes approximately self-similar, because the postshock variables including the CR pressure approach time-asymptotic values while the shock structure broadens linearly with time as  $l_{\text{shock}} \sim u_s t / 8$  and the maximum CR momentum increases approximately as  $p_{\text{max}} \approx l_{\text{shock}} u_s / \kappa_{\eta}$ . This behavior develops because the thermal leakage injection rate is controlled mainly by the shock Mach number and because the ratio  $t_{\text{acc}}/t_d$  is a function of shock Mach number. The self-similar behavior is independent of the assumed diffusion coefficient. When the drift and dissipation of Alfvén waves in the upstream region are included, the CR acceleration is less efficient for a given Mach number, as expected from previous studies [22,8]. However, at sufficiently high Mach numbers it appears, even with the inclusion of the Alfvén wave terms, that the efficiency probably asymptotes to approximately 50% as measured by both the fraction of energy flux transferred to CRs and the fraction of momentum flux that appears as postshock CR pressure.

We summarize here the main properties of our improved simulations including Alfvén wave effects:

1. The postshock pressures,  $P_c$  and  $P_g$ , approach time-asymptotic values quickly. At sufficiently strong shocks the postshock CR pressure is about 50 % of the shock ram pressure, while the normalized gas pressure drops from its gasdynamic value of 75 %. The normalized postshock gas pressure scales approximately inversely with the compression through the shock. The resulting total pressure in a strong CR modified shock will be reduced from that in an ordinary gas shock of the same initial Mach number. Typically a fraction of  $\xi = 10^{-4} - 10^{-3}$  of the incoming thermal particles become CRs through thermal leakage.
2. A significant shock precursor develops in response to nonlinear feedback from the CR pressure, so that the subshock weakens to  $M_{\text{subshock}} \sim 3$  for the initial shock Mach number  $M_0 \geq 5$ . The subshock strength increases very slowly with total Mach number in a balance between energy extracted by CRs and heating of the precursor.
3. In our present simulations heating in the precursor is dominated in strong shocks by Alfvén wave dissipation. The resulting asymptotic density compression factor through the precursor can be approximated by  $\sigma_p \sim 1.5(M_0/10)^{0.29}$  for  $M_0 \gtrsim 3$ , while the compression over the total transition can be approximated by  $\sigma_t \sim 4.9(M_0/10)^{0.33}$  for  $M_0 \gtrsim 5$ . This behavior is consistent with simple theoretical expectations. Of course, both  $\sigma_s$  and  $\sigma_t$  take gasdynamic values for smaller  $M_0$ .
4. Both the CR momentum distribution at the shock,  $g(x_s, p) = f(x_s, p)p^4$ ,

and the integrated distribution,  $G(p) = \int dxg(x,p)$ , clearly exhibit characteristic concave curvature, reflecting the nonlinear velocity structure in the precursor. At non-relativistic momenta  $G(p) \propto p^{-\alpha}$  with  $4.5 < \alpha < 4.2$ , reflecting the strength of weaker subshocks, while it flattens toward the highest momenta. Despite strong nonlinearity in the shock structures, the maximum CR momentum still scales reasonably close to predictions from test-particle theory. This behavior allows the shock precursor to evolve in an approximately self-similar manner.

5. The CR energy ratio  $\Phi(Ms)$  increases with  $M_0$  for modest Mach numbers and depends on  $\epsilon_B$ , and the ratio  $\theta = E_B/E_{th}$ . At sufficiently high Mach number  $\Phi$  asymptotes towards  $\sim 0.5$ . Since acceleration efficiency is reduced by Alfvén wave effects, higher Mach numbers are required to approach this limit as  $\theta$  increases. For larger  $\epsilon_B$  in the thermal injection model, the magnetic turbulence is weaker, so that particles can stream upstream more easily. CR injection is then more efficient. The importance of this effect is significant only in relatively weak shocks. The presence of pre-existing CRs is equivalent to a higher injection rate. In weak shocks this translates into an apparently enhanced acceleration efficiency as measured by the fraction of energy incorporated into CRs. This influence is small in strong shocks, however.

## Acknowledgments

The authors would like to thank D. Ryu for suggesting the idea of a comoving grid for CRASH code. HK was supported by the Korea Research Foundation Grant funded by Korea Government (MOEHRD, Basic Research Promotion Fund) (R04-2004-000-100590) and by KOSEF through the Astrophysical Research Center for the Structure and Evolution of Cosmos (ARCSEC). TWJ is supported at the University of Minnesota by NASA grant NNG05GF57G, NSF grant Ast-0607674 and by the Minnesota Supercomputing Institute.

## References

- [1] Achterberg, A. *Astron. & Astrophys.* 98 (1982) 195
- [2] Achterberg, A. & Blandford, R. D. *M.N.R.A.S.* 218 (1986) 551
- [3] Aharononian, F. A. et al. *Nature* 432 (2004) 75
- [4] Amato, E. & Blasi, P. *M.N.R.A.S.* 364 (2005) L76
- [5] Beck, R. *Space Sci. Rev.* 99 (2001), 243

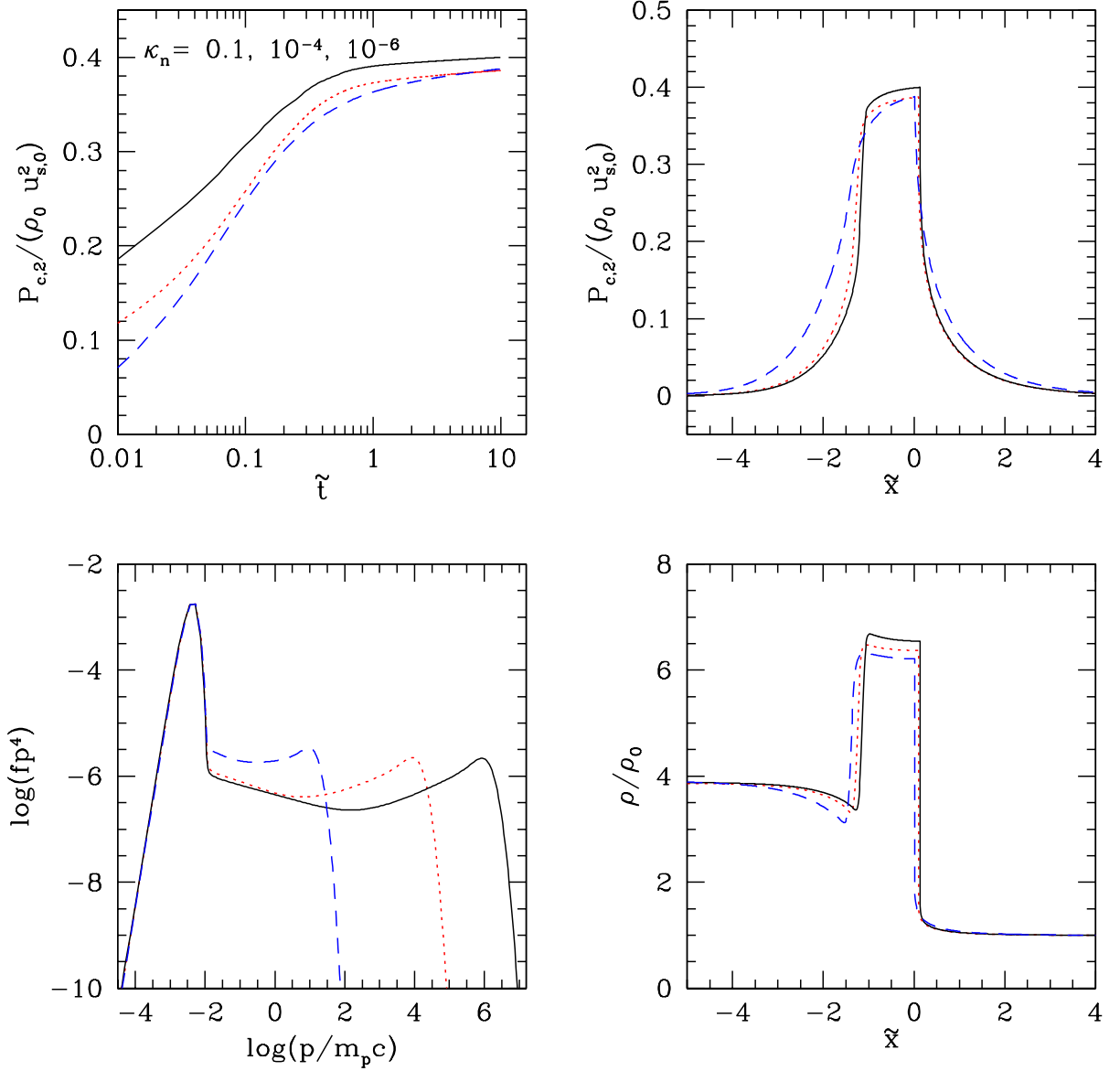


Fig. 1. *Upper left panel:* Time evolution of the postshock CR pressure for three shocks with  $M_0 = 20$ ,  $T = 10^6 \text{K}$  and  $\theta = 0.1$ . Three models with different values of  $\tilde{\kappa}_n = 0.1$  (dashed line),  $10^{-4}$  (dotted line), and  $10^{-6}$  (solid line) are shown for comparison. *Lower left panel:* The CR distribution function at the subshock,  $g(p, x_s) = f(p, x_s)p^4$ , is plotted for the three models at  $\tilde{t} = 10$ . Also spatial profiles of the CR pressure and density for the three shock models are shown in the upper right and lower right panels, respectively. The normalization scales are defined in the text.

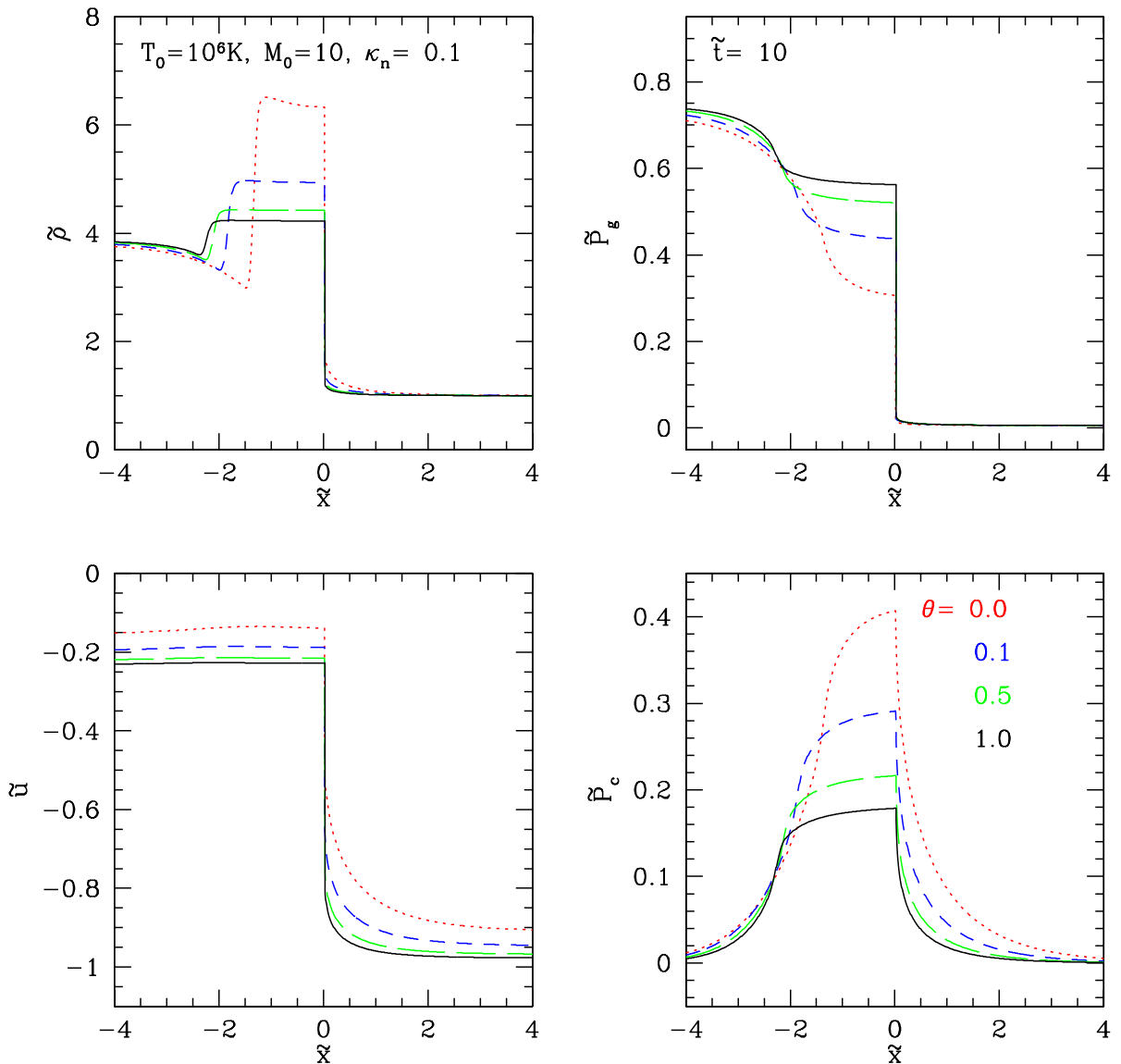


Fig. 2. Time asymptotic structure of a  $M_0 = 10$  CR-modified shock illustrating the role of Alfvén wave drift and dissipation in determining shock properties. Four models with  $\theta = 0$  (dotted line), 0.1 (dashed), 0.5 (long dashed), and 1.0 (solid) are shown. As described in the text,  $\theta = E_B/E_{th,0} = (5/9)(M_0/M_A)^2$ .

[6] Bell, A. R. M.N.R.A.S. 182 (1978) 147  
 [7] Berezhko E.G., Ksenofontov, L. & Yelshin, V. Nuc. Phys. B 39A (1995) 171  
 [8] Berezhko, E.G. & Völk, H.J. Astroparticle Physics 7 (1997) 183  
 [9] Berezhko E. G. & Ellison, D. C. Astrophys. J. 526 (1999) 385  
 [10] Blandford, R. D., and Eichler, D. Phys. Rept. 154 (1987) 1

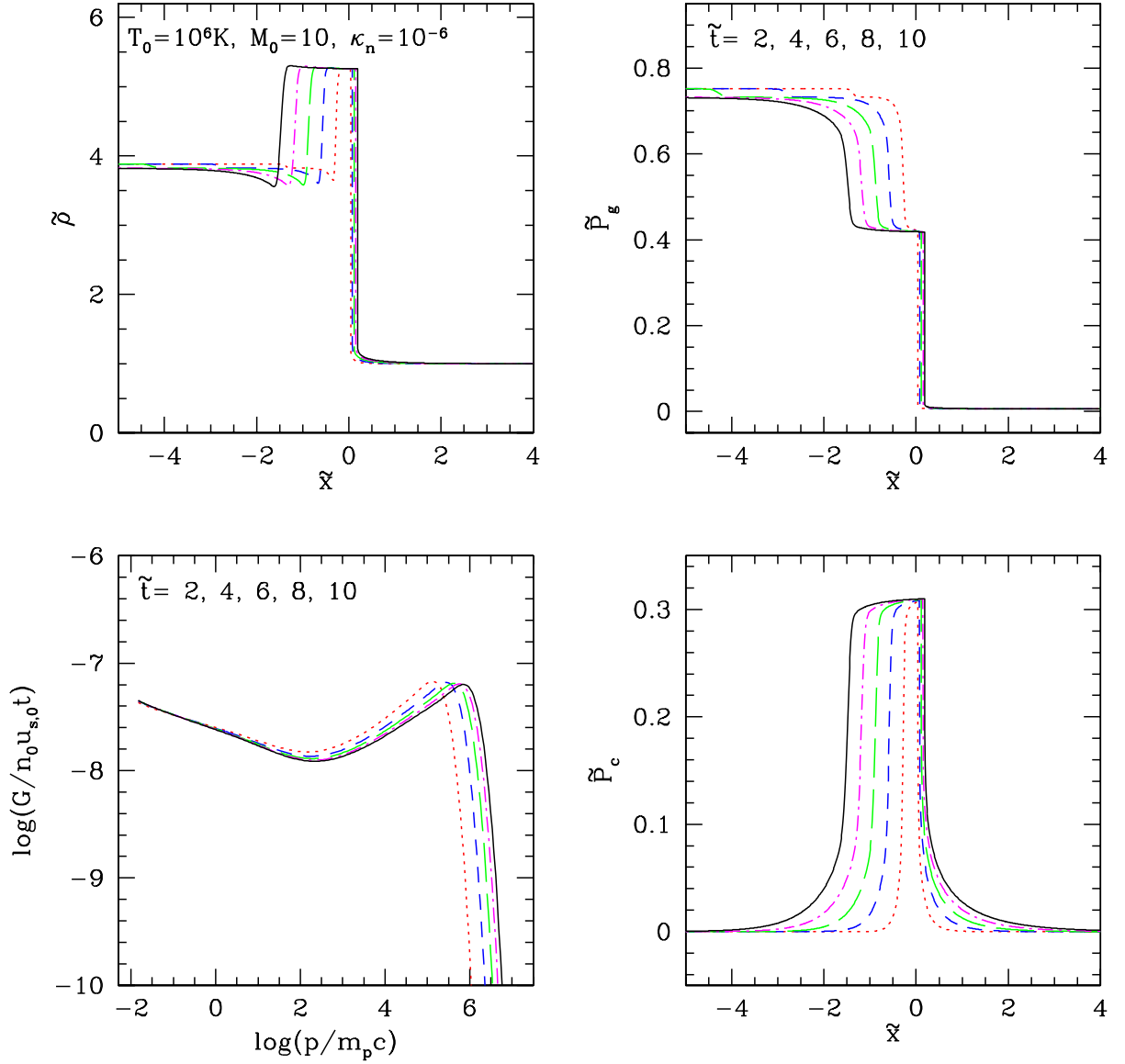


Fig. 3. Evolution of a plane-parallel shock with  $M_0 = 10$  and  $T = 10^6\text{K}$  ( $u_s = 1500 \text{ km s}^{-1}$ ) is shown for  $\tilde{t} = 2, 4, \dots, 10$ . The initial,  $\tilde{t} = 0$ , gas shock is set at rest in the computational grid by Rankine-Hugoniot shock jump condition. The injection parameter for thermal leakage injection is  $\epsilon_B = 0.2$  and the diffusion coefficient is  $\tilde{\kappa}_{BL} = 10^{-6}p$ . The Alfvén parameter,  $\theta = 0.1$ . The lower left panel shows the volume integrated CR spectrum,  $G(p) = \int dx f(x, p) p^4$  in terms of the number of particles passed through the shock,  $n_0 u_{s,0} t$ .

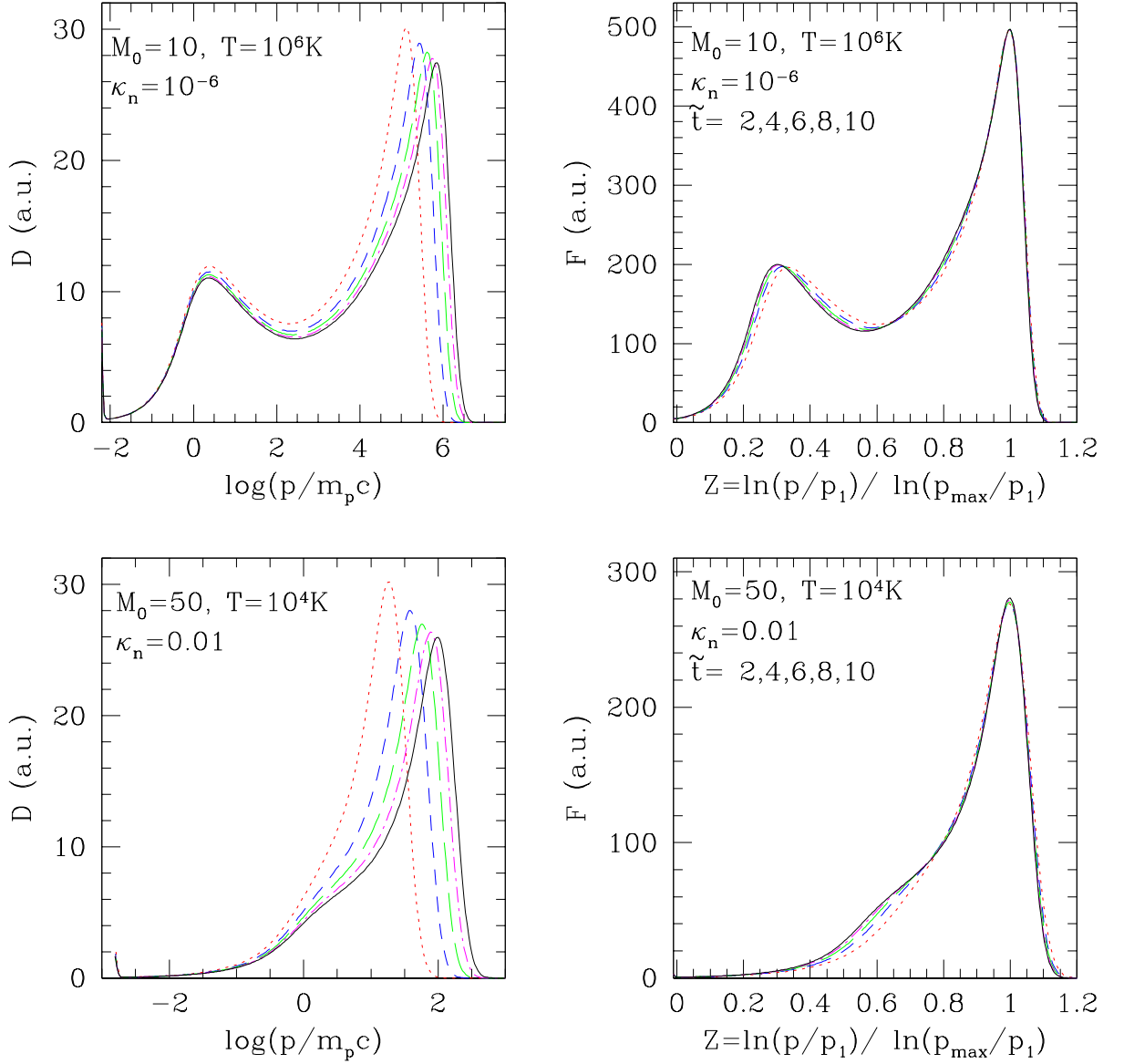


Fig. 4. The partial pressure functions  $D(p, x_s)$  and  $F(Z, x_s)$  (in arbitrary units) at the subshock are shown at  $\tilde{t} = 2, 4, \dots, 10$ . Upper panels are for the model shown in Fig. 3, while lower panels are for the model with  $M_0 = 50$ ,  $T_0 = 10^4 \text{K}$ ,  $\tilde{\kappa}_B = 0.01p/\sqrt{p^2 + 1}$  and  $\theta = 0.1$ . See text for the definitions of the momentum similarity variable  $Z$  as well as  $D(p)$  and  $F(Z)$ .

[11] Blasi, P. Amato, E. & Caprioli, D. M.N.R.A.S. 375 (2007) 1471

[12] Carilli C. L., & Taylor G. B. ARAA 40 (2002) 319

[13] Drury, L. O'C. Rept. Prog. Phys. 46 (1983) 973

[14] Drury, L. O'C., Völk, H. J. & Berezhko, E. G. Astron. & Astrophys. 299 (1995)



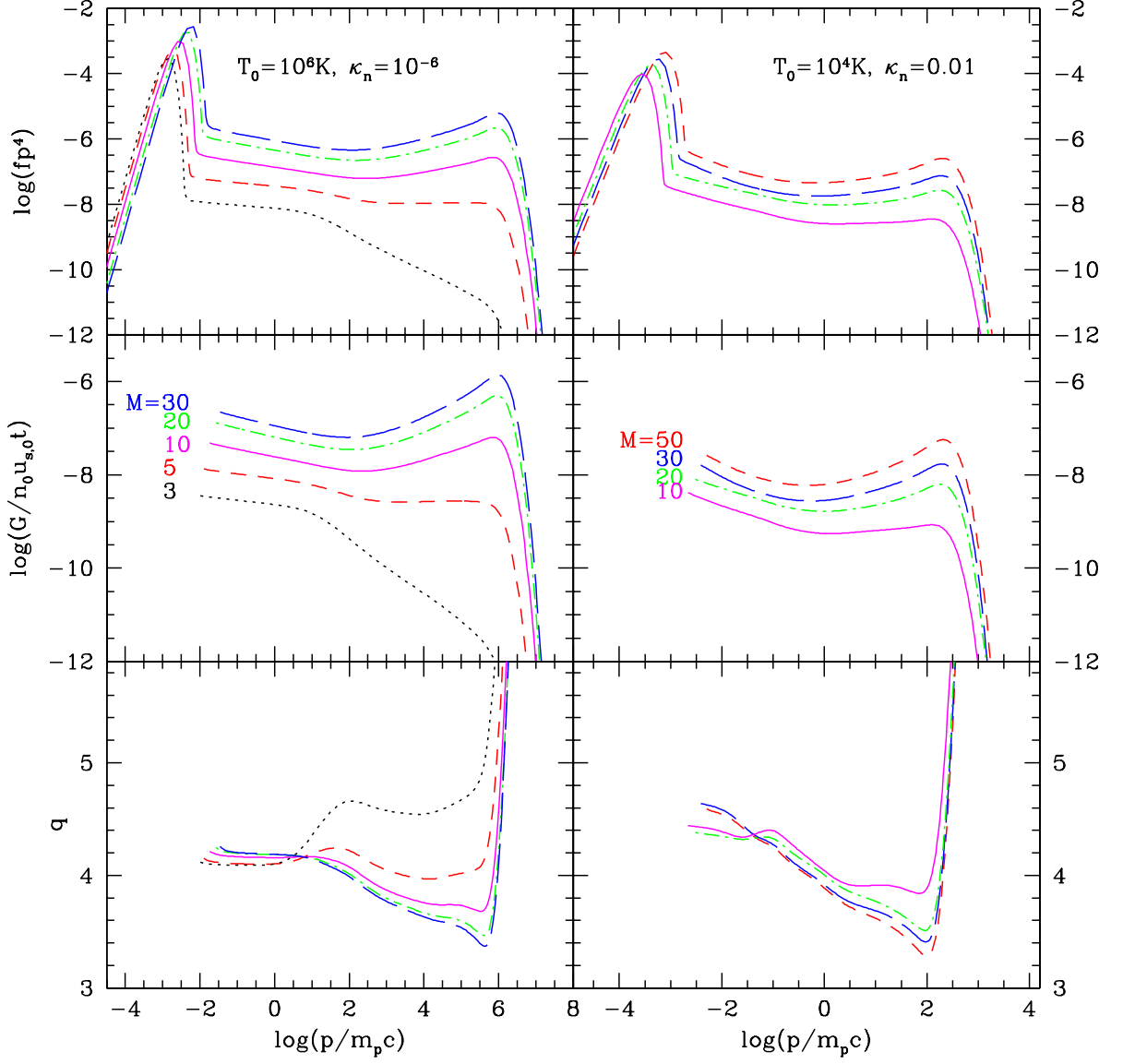


Fig. 5. CR spectrum at the shock,  $g(x_s, p) = f(x_s, p)p^4$ , the volume integrated distribution,  $G = \int dxg(x, p)$ , and  $q = -d(\ln G)/d \ln p + 4$  at  $\tilde{t} = 10$  are plotted for the models with  $\theta = 0.1$ . Left panels show models with  $T_0 = 10^6\text{K}$ ,  $\tilde{\kappa}_{BL} = 10^{-6}p$ , and  $3 \leq M_0 \leq 30$ , while right panel show models with  $T_0 = 10^4\text{K}$ ,  $\tilde{\kappa}_B = 0.01p/\sqrt{p^2 + 1}$ , and  $10 \leq M_0 \leq 50$ .

299

[15] Drury, L. O'C., Duffy, P. & Kirk, J. G. *Astron. & Astrophys.* 309 (1996) 1002

[16] Ellison, D. C., Baring, M. G. & Jones, F. C. 1995, *Astrophys. J.* 453 (1995) 873

[17] Ellison, D. C. & Berezhko, E. G. 26th ICRC 4 (1999) 446

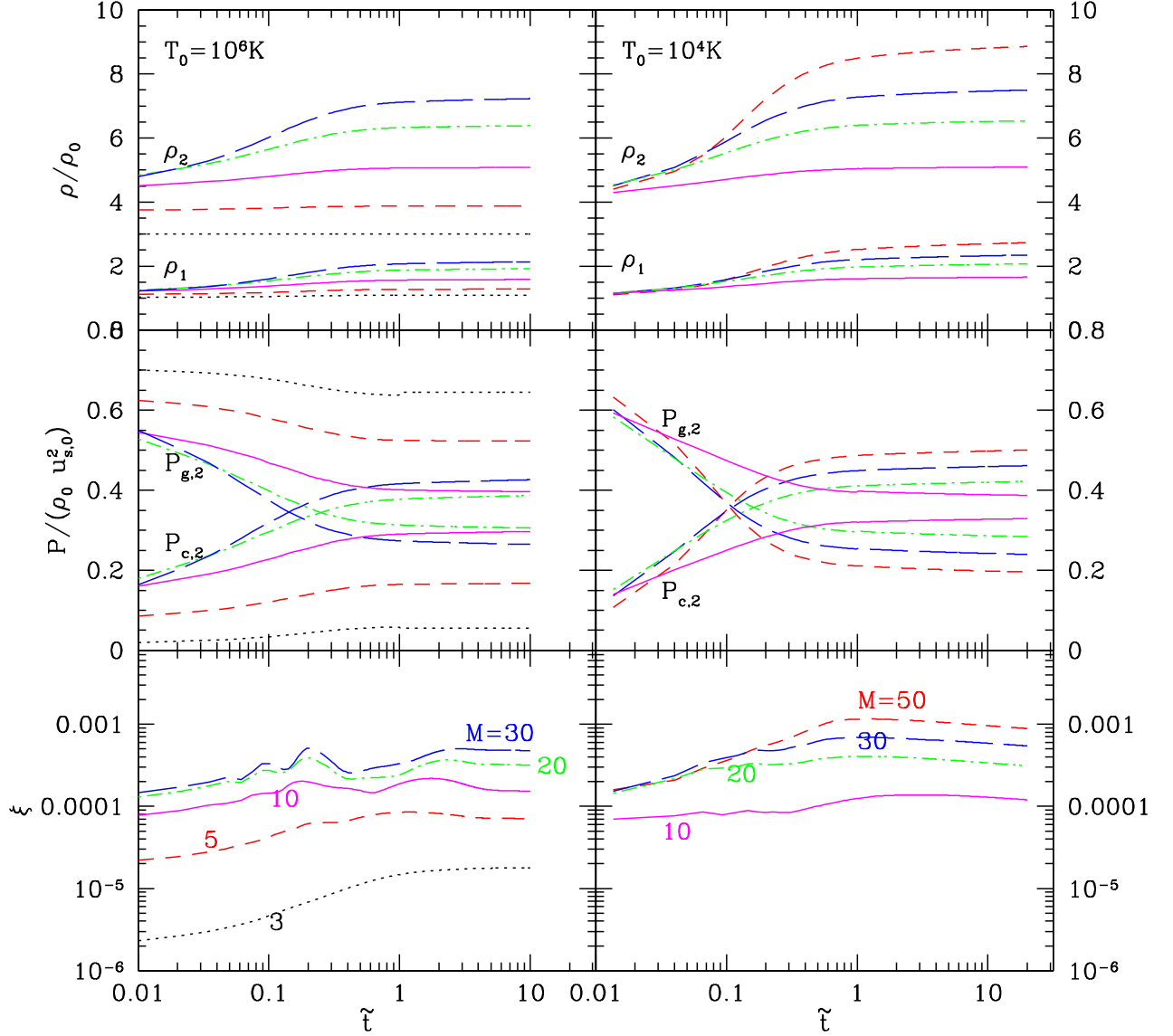


Fig. 6. Precursor compression factor,  $\sigma_p = \rho_1/\rho_0$ , total compression factor,  $\sigma_t = \rho_2/\rho_0$  ( $\rho_0 = 1$ ), postshock CR and gas pressure in units of the shock ram pressure, and the injection efficiency  $\xi$  are plotted as functions of time for the models shown in Fig. 5.

[18] Ellison, D. C., Decourchelle, A., Ballet, J. *Astron. & Astrophys.* 429 (2005), 569

[19] Ellison, D. C. & Eichler, D. *Phys. Rev. Lett.* 55 (1985) 2735

[20] Fabian, A. C. *ARAA*, 32, (1994) 277

[21] Gieseler, U. D. J., Jones, T. W. & Kang, H. *Astron. & Astrophys.* 364 (2000)

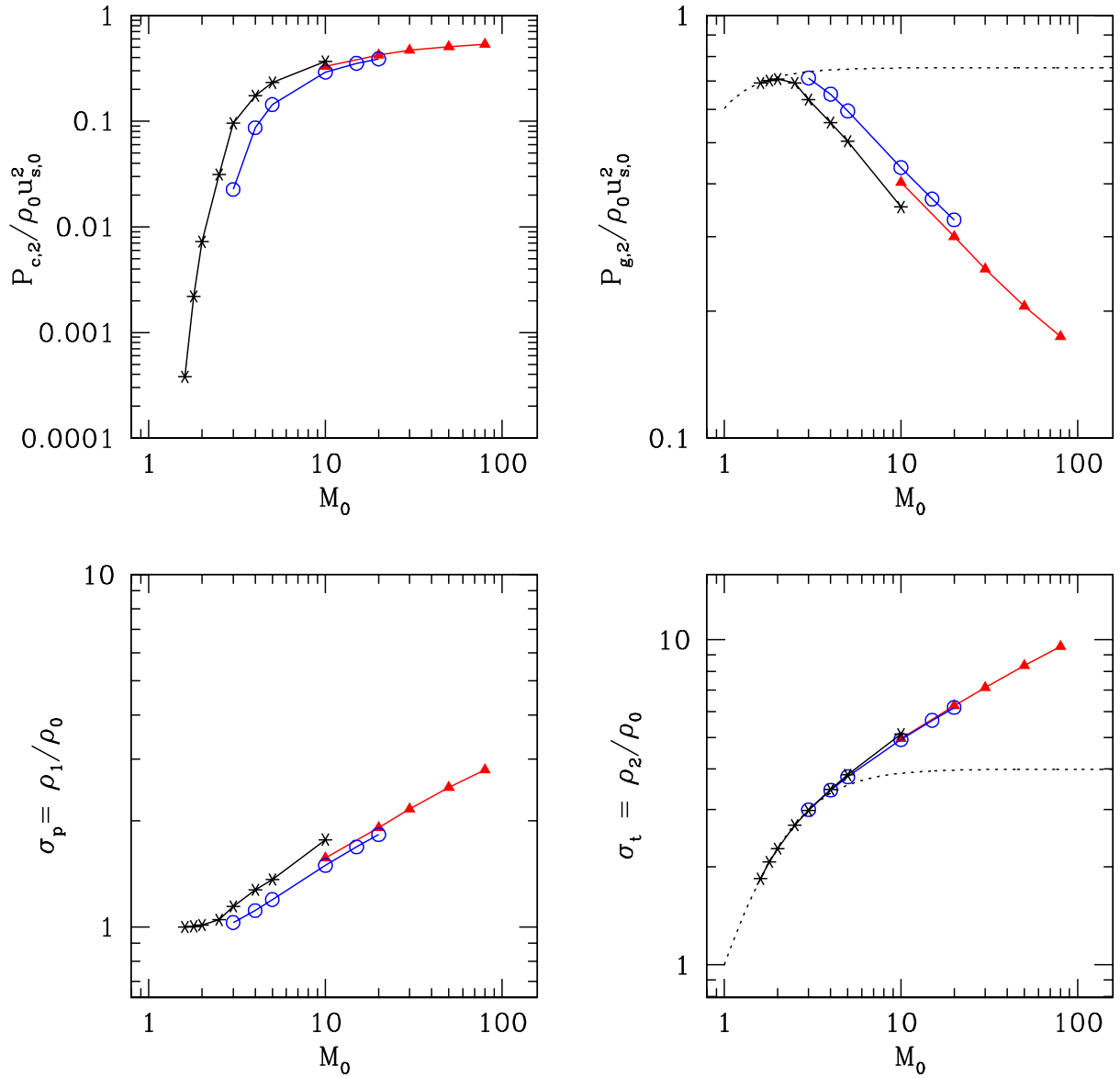


Fig. 7. Time asymptotic values of the postshock CR and gas pressure in units of the shock ram pressure, precursor compression factor,  $\sigma_p$ , and total compression factor,  $\sigma_t$ , are plotted as functions of the shock Mach number. All models use  $\theta = 0.1$ . The dotted lines represent  $P_{g,2}$  and  $\sigma_t$  calculated from the Rankine-Hugoniot relation with  $\gamma = 5/3$ . Symbols are used as follows: open circles for models with  $T_0 = 10^6$ K and  $\epsilon_B = 0.2$ , stars for models with  $T_0 = 10^6$ K and  $\epsilon_B = 0.25$ , and filled triangles for models with  $T_0 = 10^4$ k and  $\epsilon_B = 0.2$ .

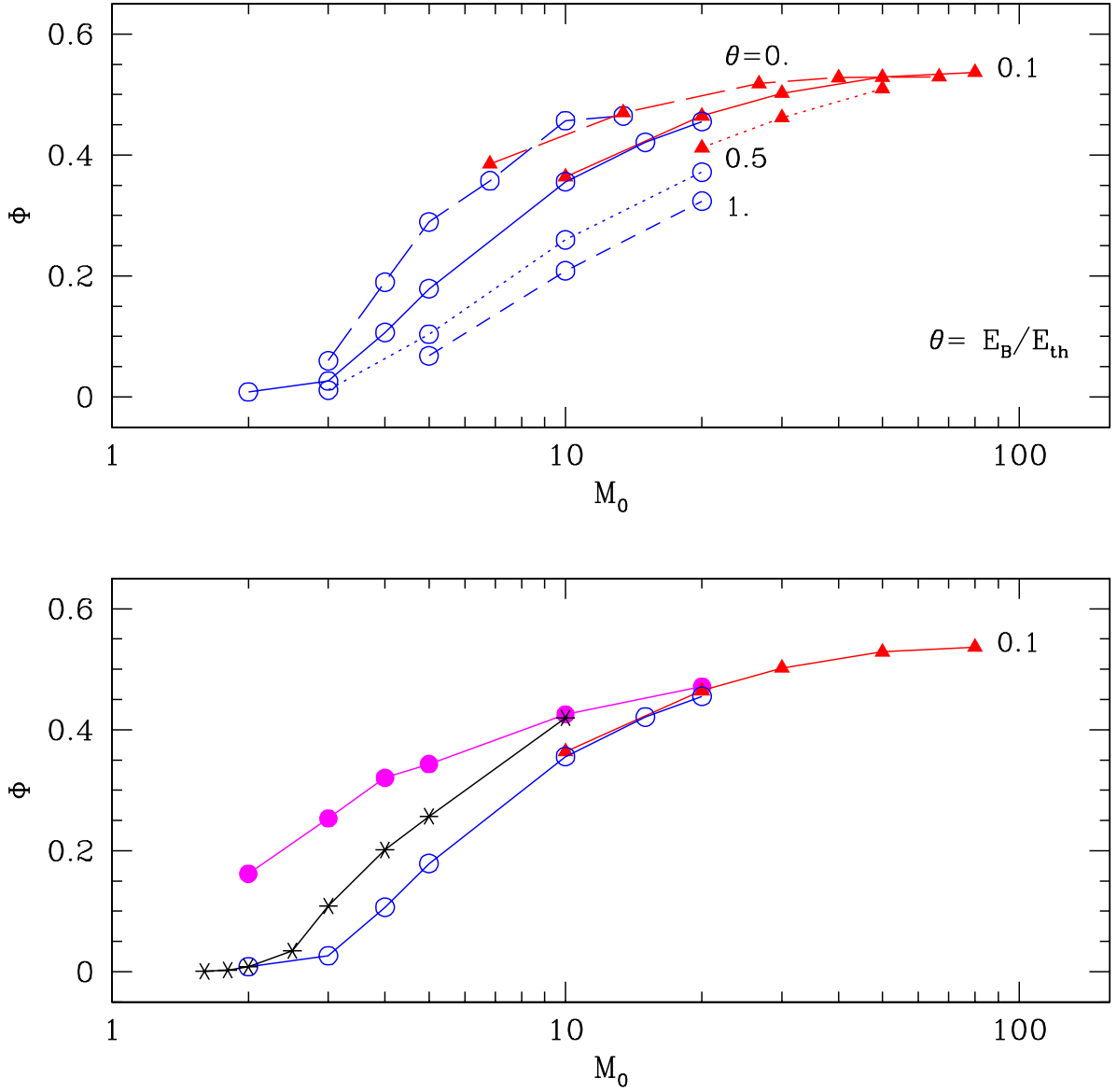


Fig. 8. The CR energy ratio  $\Phi$  is plotted as a function of the shock Mach number for different models. In the top panel,  $\epsilon_B = 0.2$  for all models, open circles are used for models with  $T_0 = 10^6\text{K}$ , while filled triangles are used for models with  $T = 10^4\text{K}$ . Long dashed lines are for  $\theta = 0.$ , solid lines for  $\theta = 0.1$ , dotted lines for  $\theta = 0.5$ , and short dashed lines for  $\theta = 1.$  cases. In the bottom panel, models with open circles and filled triangles are the same as in the top panel and shown only to be compared with other cases. Filled circles connected with the solid line are for models with  $T_0 = 10^6\text{K}$ ,  $\epsilon_B = 0.2$ , and  $\theta = 0.1$  with a pre-existing CR population with  $P_{c,0}/P_{g,0} = 0.25 - 0.5$  and  $f(p) \propto p^{-5}$ . Stars connected with the solid line:  $T_0 = 10^6\text{K}$ ,  $\epsilon_B = 0.25$ , and  $\theta = 0.1$ .

- [22] Jones, T. W. *Astrophys. J.* 413 (1993) 619
- [23] Kang, H. & Jones, T. W., *M.N.R.A.S.* 249 (1991) 439
- [24] Kang, H., Jones, T. W., and Ryu, D. *Astrophys. J.* 385 (1992) 193
- [25] Kang, H., Jones, T. W., LeVeque, R. J., Shyue, K. M. *Astrophys. J.* 550 (2001) 737
- [26] Kang, H., Jones, T. W., & Gieseler, U.D.J. *Astrophys. J.* 579 (2002) 337
- [27] Kang, H. & Jones, T. W., *Journal of Korean Astronomical Society*, 35 (2002), 159
- [28] Kang, H., *Journal of Korean Astronomical Society*, 36 (2003), 1
- [29] Kang, H., & Jones, T. W. *Astrophys. J.* 620 (2005) 44
- [30] Kang, H., & Jones, T. W. *Astropart. Phys.* 25 (2006) 246
- [31] Lagage, P. O. & Cesarsky, C. J. *Astron. & Astrophys.* 125 (1983) 249
- [32] Lucek, S. G. & Bell, A. R. *M.N.R.A.S.* 314 (2000) 65
- [33] Malkov, M. A. *Astrophys. J.* 485 (1997) 638
- [34] Malkov M.A. *Phys. Rev. E*, 58 (1998) 4911
- [35] Malkov, M. A. & Diamond, P. H. *Astrophys. J.* 642 (2006) 244
- [36] Malkov, M.A., & Drury, L.O'C. *Rep. Progr. Phys.* 64 (2001) 429
- [37] Malkov, M.A., and Völk, H.J. *Adv. Space Res.* 21 (1998) 551
- [38] McKee, C. F., and Ostriker, J. P. *ApJ*, 218 (1977) 148
- [39] Pfrommer, C., Springel, V., Ensslin, T. A., & Jubelgas, M., *Mon. Not.R. Astron. Soc.*, 367 (2006) 113
- [40] Ptuskin, V. S. & Zirakashvili, V. N. *Astron. & Astrophys.* 403 (2003) 1
- [41] Röttgering, H.J.A., Wieringa, M.H., Hunstead, R. W. & Ekers, R.D *M.N.R.A.S.* 290 (1997) 577
- [42] Skilling, J., *Mon. Not.R. Astron. Soc.*, 223 (1975) 353
- [43] Spitzer, L., *ARAA*, 28 (1990) 71
- [44] Vladimirov, A., Ellison, D. C., & Bykov, A. *Astrophys. J.* 652 (2006) 1246